JOURNAL OF SOLID STATE CHEMISTRY 98, 278–290 (1992)

Subtleties of Structure and Bonding in Ta–S–Se and Ta–Nb–S Solid Solutions

K. S. NANJUNDASWAMY AND TIMOTHY HUGHBANKS*

Department of Chemistry, Texas A&M University, College Station, Texas 77843-3255

Received August 29, 1991; in revised form December 2, 1991

Substitution of selenium by sulfur and tantalum by niobium into the $^{1}_{\infty}$[Ta_5Ta] chains characteristic of Ta_3S_2 and Ta_2S is attempted in an effort to understand the structural diversity of a metal-rich chalcogenides. Neither Ta_2S nor Ta_3S_2 incorporates a significant amount of selenium, while Ta_2Se-like structures are found to persist in $Ta_2S_{1-x}Se_x$ for $0.2 \leq x \leq 1.0$, a and c progressively increasing with x. The Ta_2Se-like structure is stable to annealing at temperatures $\geq$1000°C for $0.5 \leq x \leq 1.0$, and compositions with $x \leq 0.5$ disproportionate to Ta_3S_2, Ta_6S, and $Ta_{1+x}Se_2$ on annealing. Both our work and research completed in Franzen's laboratories show that niobium substitution into the $^{1}_{\infty}$[Ta_5Ta] chains does not occur to any large extent, instead layered Ta_2Se-like structures (M_4S_2 and M_5S_2) are stabilized. At the composition $Ta_{2-x}Nb_xS$ ($x = 0.6$) as-cast samples are virtually single phase, adopting a Ta_2Se-like structure. A single crystal structure determination for a crystal with composition $Ta_{1.4}Nb_{0.6}S$ was carried out: space group $P4/nmm$ (No. 129), $a = 3.339(1)$, $c = 9.089(7)$ Å, $V = 101.33(9)$ Å^3, $Z = 2$. While electronic structure calculations nicely rationalize the metal–metal bonding in any of these structures, the ability to predict which structures will be stabilized for which systems remains out of reach.

Introduction

Metal-rich chalcogenides of niobium and tantalum show surprising structural diversity. Franzen and Smeggil discovered the metal-rich sulfides Ta_6S and Ta_2S more than 20 years ago. These compounds feature chains in which Ta_5 pentagons are alternately stacked into chains and centered by additional Ta atoms in the pentagonal antiprisms so generated (*1–3*). Thus, the centering metal atoms are in a somewhat compressed icosahedral environment. In our laboratory, we have discovered a new tantalum-rich sulfide Ta_3S_2 which also incorporates $^{1}_{\infty}$[Ta_5Ta] units that are linked in a way similar to Ta_2S (*4–6*). In the known binary tantalum sulfides the interlayer spacing between pentagons is in the range 2.62–2.80 Å (2.64 Å in monoclinic-Ta_6S, 2.62 Å in triclinic-Ta_6S, 2.79 Å in Ta_2S, 2.80 Å in Ta_3S_2) (*1–3*). Sulfur surrounds the $^{1}_{\infty}$[Ta_5Ta] chain so as to cap alternant exposed triangular faces. Ternary representatives of these tantalum-rich sulfides are the substitutional phases $M_xTa_{6-x}S$ [M = V, Cr; $x \leq 2.5$] in which vanadium or chromium substitute for tantalum within the $^{1}_{\infty}$[Ta_5Ta] chains of Ta_6S structure (*7*).

Alternative structural motifs can be found in other ternary compounds. Tricapped trigonal prismatic tantalum chains are centered with Fe, Co, or Ni ($=M$) atoms in $Ta_9S_6M_2$ and $Ta_{11}Se_8M_2$ (*8–10*). There is a

* To whom correspondence should be addressed.

0022-4596/92 $5.00

distinct structural similarity between the fivefold symmetric, tantalum centered chains known for the Ta-rich sulfides and the fourfold symmetric chains found in Ta_4ZTe_4 (Z = Al, Si, Cr–Ni) series of compounds discovered in DiSalvo's laboratories (*11*). The $^1_\infty[M_4Si]$ core present in these truly one-dimensional materials may be viewed as intermediate between those in $InMo_3Te_3$ ($^1_\infty[Mo_3]$) and those in tantalum sulfides ($^1_\infty[Ta_5Ta]$) (*12, 13*).

That ternary compounds should exhibit structural variability is no surprise, but a more difficult problem arises when we try to understand why isoelectronic compounds such as Ta_2S, Ta_2Se, and Nb_2Se should each display unique structures. Ta_2Se, recently discovered by Harbrecht, has a layered structure which is related to the body-centered cubic Ta (*14*). The Nb_2Se structure consists of *cis* edge-condensed Nb_6 octahedra to form double chains that are cross-linked as indicated in Fig. 4, below. In Ta_2S, metal–metal bonding extends within and between the structure's imbedded icosahedral clusters, this latter description being an alternative formulation for the $^1_\infty[Ta_5Ta]$ chains mentioned above. Each of these isoelectronic compounds adopts a unique structure, differing also with the compounds Ti_2S, Ti_2Se, Zr_2S, and Zr_2Se (all having the Ta_2P structure) (*1, 16*). Neither V_2S nor Nb_2S are, as yet, known.

Structures of (Ta–Nb)-rich sulfides resemble neither Ta–S nor Nb–S binaries. Franzen and co-workers have shown recently that $Ta_{3.28}Nb_{1.72}S_2$ adopts a layer structure similar to Ta_2Se (*17*), while $Ta_{6.08}Nb_{4.92}S_4$ has a structure more similar to niobium-rich sulfides, despite having a higher tantalum to niobium molar ratio (*18*). In order to gain some better understanding of the reasons underlying this unexpected structural variability, we have studied sulfur and selenium solid solutions of metal-rich niobium and tantalum compounds and also substitutional effect of niobium into $^1_\infty[Ta_5Ta]$ chains of Ta_3S_2 and Ta_2S.

Experimental Results

Syntheses. Materials with the compositions $Ta_2S_{1-x}Se_x$ ($0 \leq x \leq 1$) were synthesized in two stages. TaS_2 and $TaSe_2$ were prepared by reacting the elements in sealed evacuated quartz tubes at 500–800°C. Cold-pressed pellets were prepared for the compositions $Ta_2S_{1-x}Se_x$ by taking Ta_2S, Ta_2Se, and Ta powders in the required stoichiometric ratio. Pellets were arc-melted (32 V, 45–50 A) at least three times on a water-cooled copper base with a nonconsumable thoriated tungsten electrode in an argon atmosphere. Extreme care must be exercised in excluding oxygen from the apparatus in these reactions, as even small amounts of oxygen contamination can lead to large sulfur mass losses in the preparation of metal-rich sulfides. The samples were "annealed" for approximately 30 sec at an arc current just adequate to sustain the arc. After cooling, the resulting buttons were weighed to monitor the mass change during reaction. The microcrystalline samples thus prepared were ground and pressed into pellets in a glove box under nitrogen atmosphere. These pellets were annealed at 1000°C inside sealed tantalum tubes lined with molybdenum foil, which in turn were contained in evacuated, sealed silica tubes. $Ta_{2-x}Nb_xS$ compositions were synthesized by arc-melting the cold-pressed pellets prepared from TaS_2, Ta, and Nb in the required stoichiometric ratios.

Powder X-ray diffraction. X-ray powder diffraction patterns were obtained with a Enraf–Nonius (FR-552) vacuum Guinier camera, with monochromated Cu$K\alpha_1$ radiation. Powdered silicon (NBS) was included in the sample as an internal standard, and the positions of the five observed lines were fit to indexed 2θ values. X-ray powder diffraction patterns were recorded for samples

before and after the annealing. Oscillation photographs were taken using a Weissenberg camera for $Ta_{2-x}Nb_xS$ crystals.

Chemical and microprobe analyses. Combustion analyses were done for polycrystalline samples of the Ta–S–Se system by air-oxidation of the samples at 800°C and weighing the white products as Ta_2O_5. Electron microprobe analyses were performed using a Cameca SX50 scanning electron microscope for Ta–Nb–S samples with Ta_2S and Ta single crystals as calibration standards.

Single crystal X-ray structure determination. After X-ray examination of several less promising candidates, a black crystal shaped as a rather irregular blade with average dimensions 0.02 × 0.02 × 0.31 mm was selected from as-cast $Ta_{1.4}Nb_{0.6}S$ samples and mounted on glass fiber with epoxy cement. (Subsequent results showed the consistently thin crystal dimension to be the [001] direction.) Preliminary examination and data collection were performed on a Nicolet R3m/V X-ray diffractometer equipped with a graphite monochromator (Mo$K\alpha$ radiation, λ = 0.71073 Å). Data collection parameters are tabulated in Table III. Cell parameters [tetragonal, *P*4/*nmm*, a = 3.3390(10) Å, c = 9.089(7) Å, V = 101.33(9) Å^3] were calculated from the least-squares fitting of the setting angles for 12 reflections ($2\theta_{avg}$ = 25.4°). (We have deviated from our usual practice of using cell constants from the Guinier powder pattern since somewhat broadened lines for these layered materials afford lower precision for powder data in this instance.) Inspection of the axial photographs taken about each axis confirmed the axis lengths and Laue symmetry. Acceptable crystal quality was indicated by inspection of the peak profiles in the ω scans for several intense reflections recorded graphically along each principal axis.

Three control reflections, collected every 97 reflections, showed no significant decay. The observed intensities were corrected for Lorentz polarization and absorption effects with an empirical absorption coefficient of 784.42 mm^{-1}. The data processing, and structure calculation were accomplished with the program SHELXTL-PLUS (Microvax II), distributed by Nicolet (*19*). The structure and thermal parameters were then refined by full-matrix least-square methods. Neutral atom scattering factors and anomalous scattering correction terms were taken from "International Tables for X-ray Crystallography" (*20*).

The space group was determined to be *P*4/*nmm* using the program SHELXS, SHELXTL-PLUS (*19*). An empirical absorption correction was applied with the maximum and minimum transmission factors of 0.9640 and 0.4400, respectively. The known Ta_2Se structure was used in devising the structural model for refinement (*14*). The refinement was initiated with a statistical distribution of Ta and Nb on both metal atom sites with the overall composition assumed to be $Ta_{1.4}Nb_{0.6}S$. Positions of all atoms and isotropic thermal parameters were refined. Following the isotropic refinement, the F_c values were calculated and used for DIFABS absorption correction for the F_o (*21*). With the sulfur atom parameters fixed, site occupancies on the metal atom sites were varied, though subject to the same constraint on the overall composition. In an attempt to then carry out a full anisotropic refinement, the U_{33} parameter on sulfur went negative and it was finally refined isotropically. The crystal data and atomic parameters are tabulated in Tables III and IV. Interatomic distances of interest appear in Fig. 7. Lists of observed and calculated structure factors are available upon request.

Results and Discussion

The marked structural differences in the isoelectronic compounds Ta_2S, Ta_2Se, and Nb_2Se are plainly evident in the depictions

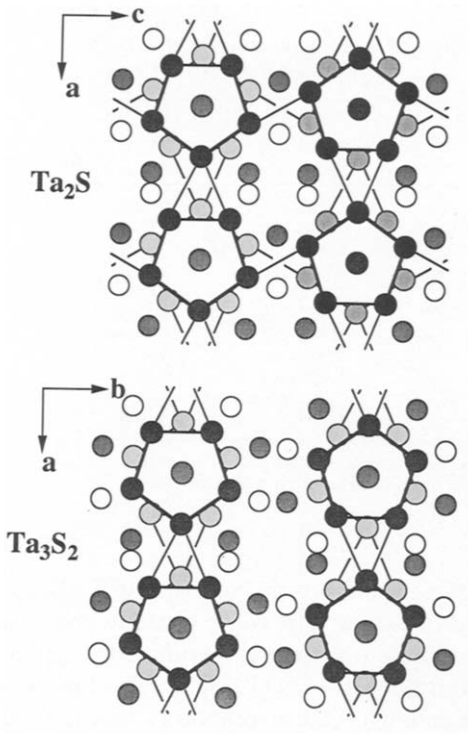

FIG. 1. The Ta_3S_2 and Ta_2S structures, projected on planes normal to the pentagonal antiprismatic chains [(001) for Ta_3S_2, (010) for Ta_2S]. Only Ta–Ta bonds within and between the pentagonal antiprisms are indicated.

shown in Figs. 1–3. Ta_3S_2 and Ta_2S can be considered as built from Ta_6S_5 chains (*6*), these being linked by formation of interchain Ta–Ta bonds resulting in two-dimensional metal–metal bonded layers. These layers are shown to extend in the *ac* planes for Ta_3S_2 and in the *ab* planes for Ta_2S. The adjacent layers are further held together by interlayer Ta–S bonds in Ta_3S_2, whereas in Ta_2S the layers are fused so as to share the sulfurs between the chain in adjacent layers, leading to an extended Ta–Ta bonded network that extends in three dimensions.

The situation is quite different in case of the Ta_2Se structure shown in Fig. 2. This compound can be thought of as derived from bcc-Ta by inserting two selenium layers after every four (100) square-net layers of Ta. The result is a two-dimensional layered compound with van der Waals gaps between adjacent Se layers. The uniqueness of the structure stems from the thickness of the Se–Ta–Ta–Ta–Ta–Se sequenced layers in this material. All atoms in the structure can be captured in [110] sections, which are also useful for comparison with bcc-Ta and the related M_5S_2 structure. This is shown in Fig. 3. The layer sequences in M_5S_2-type structure ($Ta_{3.28}Nb_{1.72}S_2$), and Ta_2Se-type structures are [S–5Ta–S] and [Se–4Ta–Se], respectively. Furthermore, these networks are held together by van der Waals forces. The structure of Nb_2Se shows little resemblance to either of the aforementioned tantalum compounds. Instead, the Nb_2Se structure is more closely related to the Ti_5Te_4-

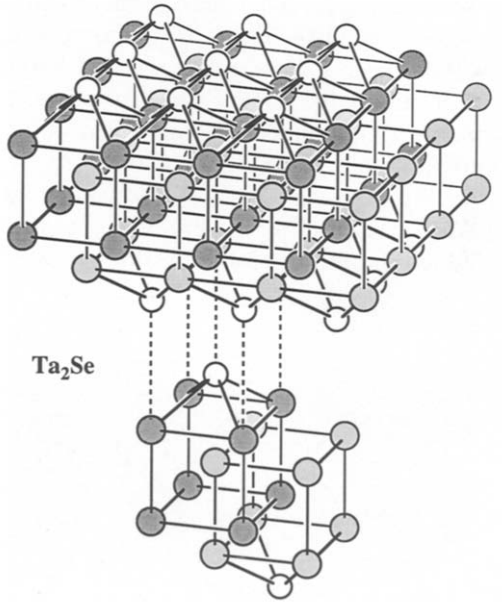

FIG. 2. The layered structure of Ta_2Se may be viewed as an insertion phase derived from bcc-Ta, in which two neighboring Ta layers of every six are replaced by selenium layers. The thick [Se–$(Ta)_4$–Se] sandwiches are held together by van der Waals interactions. Large circles: Ta; small circles: Se.

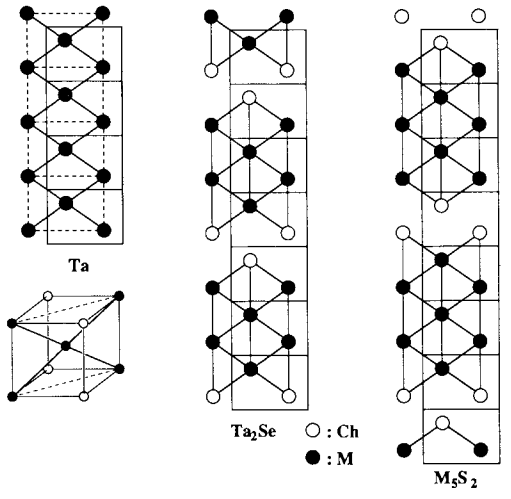

FIG. 3. [110] sections of the bcc-Ta, M_4S_2 (Ta_2Se) and M_5S_2 ($Ta_{3.28}Nb_{1.72}S_2$) structures.

TABLE I

UNIT CELL PARAMETERS FOR $Ta_2S_{1-x}Se_x$ ($0 \leq x \leq 1$) COMPOSITIONS

Composition (x)	Cell parameters (Å)			Structure type
	a	b	c	
1.0	3.371(2)		9.826(3)	Ta_2Se
0.875	3.368(2)		9.775(9)	
0.75	3.361(3)		9.706(21)	
0.70	3.356(1)		9.701(9)	
0.60	3.351(2)		9.659(10)	
0.50	3.343(3)		9.570(4)	
0.40	3.334(1)		9.414(8)	
0.25	3.333(8)		9.365(3)	
0.20	3.329(9)		9.33(7)	
0.10	7.392(11)	5.575(11)	15.25(3)	Ta_2S
0.0	7.381(6)	5.583(10)	15.19(4)	

Note. Compositions in the range $0 \leq x < 0.5$ are metastable and disproportionate on annealing below 1200°C.

type structure (*22, 23*). The Nb_2Se structure consists of crosslinked double chains of fused $^1_\infty[Nb_5Se_4]$ units sharing the *cis* edges as shown in Fig. 4. There are no compounds in the Ta–X (X = S,Se) system known which adopt the Ti_5Te_4-type structure, although the ternary compound $Ta_5Ni_4P_4$ is known with a Ti_5Te_4-related structure (*24*).

In attempts to substitute selenium into Ta_2S and Ta_3S_2, we observed no evidence of selenium incorporation. Although X-ray powder diffraction patterns of $Ta_2S_{0.9}Se_{0.1}$ did not show any Ta_2Se present, the lattice parameters were not significantly different from that of Ta_2S (Table I). The fate of the selenium in these reactions has not been ascertained, but we note that the Ta walls of the container are often more involved in selenium reactions than in pure sulfide preparations.

The Ta_2Se-like structure persists in $Ta_2S_{1-x}Se_x$ for $0.2 \leq x \leq 1.0$. End members in the $Ta_2S_{1-x}Se_x$ series are synthesized above 1500°C. Ta_2Se was originally obtained only by arc-melting reactions; Ta_2S was made either by arc-melting or by heating elements in the required stoichiometry above 1500°C. We also are able to synthesize Ta_2Se by combining $TaSe_2$ and Ta in the required stoichiometric ratio into pellets and allowing them to react for 1–2 weeks at 1000°C. Reactions are carried out in tantalum tubes sealed under an argon atmosphere with the pellet being wrapped in a molybdenum foil in order to reduce the attack on walls of the tantalum container. Lattice parameters for the product obtained are, within experimental error, the same as that obtained from arc-melting reactions. Although this method yields better crystalline products compared to the arc-

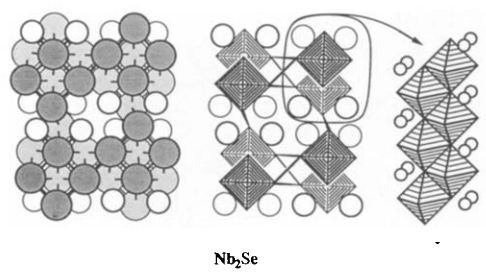

FIG. 4. The Nb_2Se structure. The structure may be viewed as built by linking of chains that are in turn formed by condensation of Nb_6Se_8 clusters into chains: $^1_\infty[Nb_2Se] \triangleq {}^1_\infty[Nb_4Se_2] \triangleq {}^1_\infty[Nb_{3/1}Nb_{3/3}Se_{4/2}]$, where $\frac{4}{2}$ Se atoms are lost through condensation of the Nb_6Se_8 clusters.

melting reactions (without subsequent annealing), the method cannot be used for synthesizing $Ta_2S_{1-x}Se_x$ ($0 \leq x \leq 0.5$) solid solutions due to the metastable nature of these sulfur-rich phases in this temperature range. In studies of lattice parameter variations, all materials $Ta_2S_{1-x}Se_x$ were formed only by arc-melting technique, while phase stabilities are studied further by annealing at different temperatures.

In the range $0 \leq x \leq 0.5$, $Ta_2S_{1-x}Se_x$ disproportionates on annealing at 1000°C for about 10 days. Careful thermodynamic measurements had revealed Ta_2S to be unstable below 1000°C and it was thought that disproportionation would yield $Ta_{1.35}S_2$ and Ta, but Ta_2S disproportionates to form products that are different than had been expected (*25*). Below 1300°C, Ta_2S disproportionation occurs to give Ta_3S_2 and Ta_6S, as indicated by our X-ray diffraction powder analyses. Chemical analyses by air-oxidation of the starting material and the products of disproportionation after annealing, as indicated by following equations, support this:

$$9\,Ta_2S \xrightarrow[\text{sealed Ta tube}]{1000°C} 4\,Ta_3S_2 + Ta_6S \quad (1)$$

$$9\,Ta_2S \xrightarrow[\text{air oxidation}]{800°C}$$

$$9\,Ta_2O_5 \xleftarrow[\text{air oxidation}]{800°C} 4\,Ta_3S_2 + Ta_6S. \quad (2)$$

In a preparation intended to make Ta_5NbS_4 starting from TaS_2, Ta, and Nb at 1300°C, we find that Ta_2S coexists with Ta_3S_2 along with other unknown phases.

The cell parameters for $Ta_2S_{1-x}Se_x$ solid solutions are given in Table I, and the variation of cell parameters as a function of x is shown in Fig. 5. For composition $Ta_2S_{1-x}Se_x$ with $x = 0.1$, although we do not see any significant deviation in the cell parameters compared to the pure Ta_2S phase indicating no significant Se incorporation, the X-ray powder diffraction patterns do not show any Ta–Se phases being present. However, for

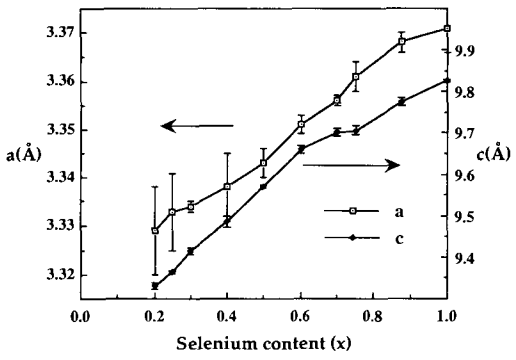

FIG. 5. Lattice parameters for $Ta_2S_{1-x}Se_x$ system.

compositions with $x > 0.1$, diffraction patterns could be indexed on a tetragonal cell similar to Ta_2Se—with no Ta_2S being present. This implies that no more than 10% of the sulfur in the Ta_2S structure type can be replaced by selenium, and there is no evidence for incorporation of selenium even at the 10% concentration. We attribute this to the steric crowding of chalcogens around the $^1_\infty$[Ta_5Ta] chains. Ta_2S and Ta_3S_2 are severely constrained by close sulfur–sulfur contacts, with some pairs of sulfides separated by only 2.86 Å in Ta_2S and 2.93 Å in Ta_3S_2. Comparison of these distances with those in $Nb_{21}S_8$ and Nb_3S_4 (3.35 ± 0.01 Å) (*26*), MoS_2 (3.16 and 3.47 Å), and similar sulfides (*27*) suggest that Ta_2S and Ta_3S_2 pay an unusually large price in sulfide–sulfide repulsions in order to gain the evidently strong metal–metal bonding offered by the $^1_\infty$[Ta_5Ta] chains. It would probably be more realistic to consider the possibility of limited *oxide* substitution rather than *selenide* substitution.

X-ray powder diffraction patterns for compositions $Ta_2S_{1-x}Se_x$, with $0.1 \leq x \leq 0.5$, are different before and after the annealing at 1000°C. Like Ta_2S itself, compounds formed at high temperature in this range of composition disproportionate on annealing. With increasing amounts of sulfur we see increasing amounts of Ta_3S_2 as one of the

disproportionation products, judging from the growth of intensity of the strong reflections of Ta_3S_2. In addition to Ta_3S_2 and Ta_6S, we also see $TaSe_2 + Ta_{1+x}Se_2$ as disproportionation products of annealing. Due to this disproportionation, the cell parameters a and c given in Table I and Fig. 5 are determined from X-ray powder diffractions of the as-cast samples. Powder diffraction patterns for solid solutions $Ta_2S_{1-x}Se_x$ in the range $0.5 \leq x \leq 1.0$ are little changed before and after annealing at 1000°C.

From the data in Table I and Fig. 5, it is clear that the cell parameters a and c decrease with decreasing selenium content in the solid solutions. The lower limit of the lattice parameters for these compositions can be estimated by assuming that Ta_2S structure adopts Ta_2Se-like structure. In this estimation, Ta–S and S–S bond distances are taken from the structure of $Ta_{3.28}Nb_{1.72}S_2$ (a five-layer modification of Ta_2Se structure) and substituted into the Ta_2Se structure. The values of a and c so estimated are respectively 3.32 and 8.98 Å.

Although from the close structural resemblance between (010) planes of Ta_3S_2 and (110) planes of Ta_2S (Fig. 1) it is reasonable to expect intergrowth between these two structures, we have not yet seen any evidence that suggests this occurs. Instead we found that Ta_2S on annealing at temperatures below 1200°C disproportionated to Ta_3S_2 and Ta_6S, while Ta_3S_2 is a stoichiometric line phase that disproportionates to Ta_2S and $Ta_{1+x}S_2$ when melted in an arc-furnace. The phases Ta_3S_2 and Ta_2S coexisted around 1300°C. If Ta_2S–Ta_3S_2 intergrowth structures are to be found, it seems likely to be stable only at temperatures above 1300°C.

Our attempts to substitute niobium for tantalum in the $^1_\infty[Ta_5Ta]$ chains of Ta_3S_2 and Ta_2S gave unexpected results. $Ta_{3-x}Nb_xS_2$ compositions when richer in tantalum resulted in Ta_3S_2, Ta_2S, and NbS_2 phases in addition to other unknown phases at temperatures below 1300°C. Thus, while niobium incorporation into the Ta_3S_2 structures cannot be ruled out, the appearance of other niobium compounds in niobium-poor preparations suggests that such incorporation must be quite limited. In reactions carried out by arc-melting, for the same composition we found NbS_2 and $Ta_{3.28}Nb_{1.72}S_2$ (M_5S_2 structure) as major phases. We continued our efforts to synthesize Nb substituted $^1_\infty[Ta_5Ta]$ chain in the Ta_2S system. Since Ta_2S is unstable at temperatures below 1200°C, we carried out all our reactions in the arc-melter. For the composition $Ta_{2-x}Nb_xS$ at $x = 0.1$, powder diffraction patterns show only the Ta_2S phase without any significant deviation in the cell parameters. However, when the intended composition is $Ta_{1.75}Nb_{0.25}S$, the presence of an M_5S_2-phase, in addition to Ta_2S, is also indicated. The fate of the excess sulfur when this more metal-rich compound is found is not apparent among the crystalline phases.

In view of the differences in the composition of the $Ta_{2-x}Nb_xS$ phase found in ours and Franzen's laboratories, we subjected our samples to microprobe analysis. Back scattered electron micrographs are shown in Fig. 6; Fig. 6a is for a sample with composition $Ta_{1.40}Nb_{0.60}S$ (prepared as outlined in the experimental section), Fig. 6b is for $Ta_{1.05}Nb_{0.95}S$. Inspection of the two micrographs leaves the clear impression of the greater homogeneity of the $Ta_{1.40}Nb_{0.60}S$ sample. Analyses of different regions of this sample are consistent with this impression, and with the composition in the case of $Ta_{1.40}Nb_{0.60}S$. Several islands with differing compositions appear in the $Ta_{1.05}Nb_{0.95}S$ sample, including a possible M_2S phase with an analyzed composition of $Ta_{2-x}Nb_xS$ ($x = 0.83 \pm 0.03$). The nominal composition of other regions in this sample suggest the possibility of even more phases in this system. Analysis of several locations in the samples indicate that the micrographs shown are representative. Of course, the

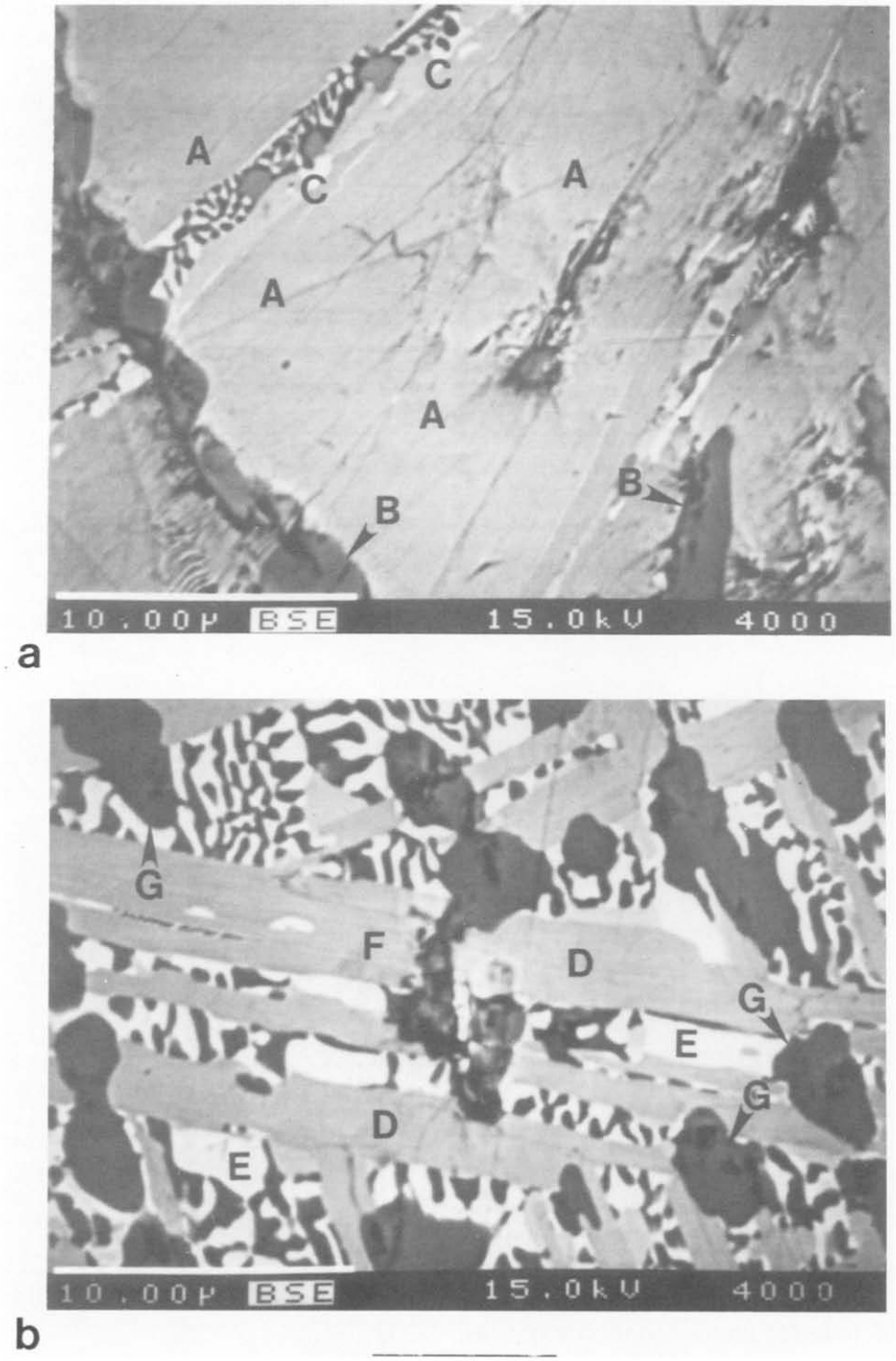

FIG. 6. Back scattered electron micrographs of samples with compositions (a) $Ta_{1.4}Nb_{0.6}S$ and (b) $Ta_{1.05}Nb_{0.95}S$. Preparation of samples is discussed in the text. A, $Ta_{2-x}Nb_xS$ ($0.55 \leq x \leq 0.6$); B, $Nb_{1-x}Ta_xS$ ($x \approx 0.3$); C, $Ta_{6-x}Nb_xS$ ($x \approx 1.4$); D, $Ta_{2-x}Nb_xS$ ($0.80 \leq x \leq 0.86$); E, $Ta_{16-x}Nb_xS$ ($x \approx 5.0$); F, $Ta_{3.3}Nb_{1.4}S$; G, $Nb_{1-x}Ta_xS$ ($x \approx 0.3$).

TABLE II

X-RAY POWDER DIFFRACTION DATA FOR $Ta_{1.4}Nb_{0.6}S$

hkl	d_{obs}	d_{calc}[a]	I_{obs}[b]
001	9.081	9.089	s
102	2.684	2.685	s
110	2.353	2.353	m
111	2.279	2.278	s
103	2.239	2.240	s
005	1.818	1.818	ww
200	1.663	1.664	s
006	1.511	1.515	ww
115	1.438	1.439	w
212	1.415	1.414	m
213	1.336	1.336	s
116	1.274	1.274	w
205	1.227	1.227	w
220	1.177	1.176	m

[a] *P4/nmm*; unit cell parameters: a = 3.328(4) and c = 9.089(19) Å.

[b] s, strong; m, medium; w, weak; ww, very weak.

Ta_2Se-like phase may have an appreciable phase width and variations in the rate of cooling may be responsible for at least some of the discrepancies in these results.

$Ta_{1.40}Nb_{0.60}S$ is isostructural with Ta_2Se described above. The single crystal results described below are quite similar in their metrical details with that reported for $Ta_{1.05}Nb_{0.95}S$ by Franzen and co-workers, with differences in bond distances and angles being statistically insignificant. Tables II and III show X-ray powder diffraction data and crystallographic data, respectively, for $Ta_{1.40}Nb_{0.60}S$.

In the ensuing, the peripheral metal layers are labeled as $M2$ and the inner layers of metal atoms as $M1$ (Fig. 7). The structure can be regarded as consisting of distorted capped cubes. The cubes consisting of four $M2$ and four $M1$ atoms are modestly contracted along c, and the $M1$ atoms contained therein are somewhat shifted toward the four (inner) $M1$ atoms. Forming the corners of the distorted cube around the inner $M1$ atoms are four $M1$ atoms at 2.83 Å and four $M2$ atoms at 2.93 Å, which are capped further by one $M2$ atom at 3.29 Å, four $M1$ atoms at 3.34 Å, and one sulfur atom at 2.67 Å. The cubes surrounding the peripheral metals atoms $M2$ consist of four $M1$ atoms at 2.93 Å and four sulfur atoms at 2.54 Å, capped by one $M1$ at 3.29 Å and four $M2$ atoms at 3.34 Å. These metals have an additional distant sulfur at 3.13 Å coming from an adjacent layer. While this is too long to imply a significant bonding interaction,

TABLE III

CRYSTALLOGRAPHIC DATA FOR $Ta_{1.4}Nb_{0.6}S$

Chemical formula	$Ta_{1.40}Nb_{0.60}S$
Color	Black
a (Å)	3.339(1)
c (Å)	9.089(7)
V (Å^3)	101.3(1)
Z	2
Formula weight	341.1
Space group	*P4/nmm* (No. 129)
T (°C)	21
λ (Å)	0.71073
Scan method	$\omega - 2\theta$
Abs. coeff. (μ) (Mo$K\alpha$)	784.42 cm^{-1}
Data collection instrument	Nicolet R3m/V
Transmission coeff. range	0.44–0.96
Crystal dimens, mm	0.02 × 0.02 × 0.31
2θ(max), deg	60
No. of reflections	
measured	1200 ($\pm h$, $\pm k$, $\pm l$)
unique	120 (R_{merge} = 6.8%)[a]
unique obsd. ($F > 3\sigma(F)$)	120 (all data); 111 ($F > 3\sigma(F)$)
No. of variables	12
R[b]; R_w[c] (%)	4.6; 5.1 (all data); 3.9; 4.6 ($F > 3\sigma(F)$)
Goodness of fit indicator	1.03
Max. (Min.) peaks in final diff. map	7.21 (−4.86) e$^-$/Å^3

[a] Following ellipsoidal correction and use of a ψ-scan, the DIFABS absorption correction was applied (*21*).

[b] $R = \Sigma(|F_o| - |F_c|)/\Sigma|F_o|$.

[c] $R_w = [\Sigma w(|F_o| - |F_c|)^2/\Sigma w|F_o|^2]^{1/2}$; $w = 1/(\sigma^2(|F_o|) + 10^{-5}|F_o|^2)$.

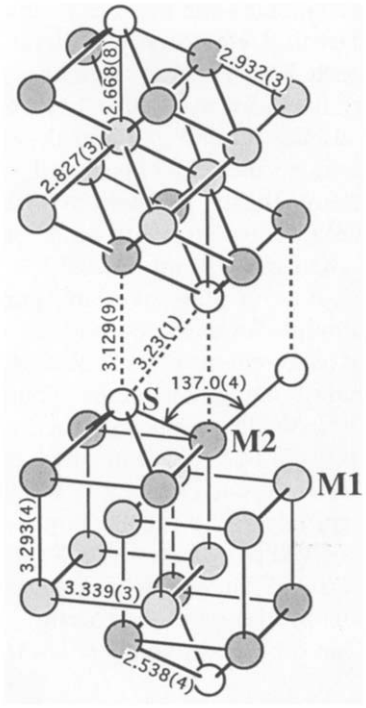

FIG. 7. Important interatomic distances for $Ta_{1.4}Nb_{0.6}S$. Different bonds are drawn in the two layers shown for visual clarity only; the fragments of the two layers shown are identical.

it is notable that the corresponding Ta–Se distance in Ta_2Se is 3.82 Å.

The shortest S–S contact within the layers is 3.34 Å, and between layers is 3.23 Å. This difference between Se–Se and S–S interlayer contacts of Ta_2Se and the M_2S structures is 0.32 Å, in reasonable agreement with the 0.28 Å one expects on the basis of crystal radii comparison (*28*). Surprisingly, the interlayer *M*–S distance spacing declines by 0.70 Å in going from the selenide to the sulfide. This is a result of a combination of factors that originate from the smaller sulfide radius. First of all, the *a* parameter is set mostly by the *M*–*M* bonding within the layers and shrinks by only 0.04 Å when Se is replaced by S (the very similar Nb and Ta radii allow us to ignore changes due to replacement of Ta by Nb). Because the M_4 squares on which the chalcogens sit are nearly the same size, the planes of the S layers in the M_2S structure are displaced only 0.95 Å from the peripheral *M*2 layer planes, while the corresponding displacement in Ta_2Se is 1.20 Å. In other words, the smaller sulfides can sink further into the surrounding square of *M*2 atoms than selenides can. Because of this, the S–*M*2–S angle opens up to 137°—compared with 126° in Ta_2Se (see Fig. 7). This leaves the M2 centers more exposed and may permit some weak interlayer *M*2–S interaction.

Franzen and co-workers have noted that because Nb occupancy is higher for sites with greater sulfur coordination in the M_2S and related M_5S_2 structures (M = Nb or Ta), Nb–S bonds may be stronger than Ta–S bonds. Our refinement indicates that the *M*1 site is occupied almost entirely by Ta, while the *M*2 site is mixed (Table IV). It is to be noted that the relative occupancies of Ta and Nb are in good agreement with Franzen's results, but our material shows a higher Ta content. Our composition of $Ta_{1.4}Nb_{0.6}S$ is based on electron microprobe analyses, with relatively little weight placed on the absolute occupancies obtained in the single crystal X-ray study. Determination of the composition using the X-ray results is inherently precarious because of unavoidable correlation between the scale factor, site occupancies, and thermal parameters. This is to be expected, since the majority of

TABLE IV

ATOMIC POSITIONS, OCCUPANCIES, AND THERMAL PARAMETERS FOR $Ta_{1.4}Nb_{0.6}S$

	Site	z	(% Ta occ.)	U_{eq}	U_{11}	U_{33}
*M*1	2*c*[a]	0.4145(2)	97.6(5)[b]	0.005(1)	0.005(1)	0.005(1)
*M*2	2*c*	0.7767(2)	76.1(5)[b]	0.008(1)	0.007(1)	0.009(1)
S	2*c*	0.1210(9)	16	0.005(2)		

[a] Site 2*c*: (⅓, ⅔, *z*).

[b] Refinement of multiplicities were constrained to yield the composition $Ta_{1.4}Nb_{0.6}S$ and are interpreted as the following mixed Ta,Nb occupancies: *M*1, 94.6% Ta + 5.4% Nb; *M*2, 45.4% Ta + 54.6% Nb.

TABLE V

PARAMETERS FOR EXTENDED HÜCKEL CALCULATIONS

	Orbital	H_{ii} (eV)	$\zeta_1{}^b$	$\zeta_2{}^b$	$c_1{}^a$	$c_2{}^a$
Nb	4*d*	−8.26	4.08	1.64	0.6401	0.5516
	5*s*	−7.92	1.89			
	5*p*	−4.15	1.85			
Ta	5*d*	−9.36	4.76	1.938	0.6105	0.6105
	6*s*	−8.64	2.28			
	6*p*	−4.75	2.24			
S	3*s*	−20.0	2.12			
	3*p*	−13.3	1.83			
Se	4*s*	−21.5	2.43			
	4*p*	−13.0	2.07			

[a] Coefficients used in double-ζ expansion.
[b] Slater-type orbital exponents.

the compound's X-ray scattering power is due to more numerous heavy metal atoms. For the refinement reported herein, the overall Ta/Nb ratio was fixed by constraining the sum of the site occupancies to correspond with a Ta : Nb ratio of 1.4 : 0.6. When the refinement was carried out by fixing the sulfur parameters and letting both metal atom site occupancies vary along with the scale factor, the residuals were essentially identical but the Ta content on both sites increased by approximately 7%. The reported deviations in the site occupancies should clearly be interpreted with prudence.

Bonding Comparison of Ta_2S, Ta_2Se, and Nb_2Se

In order to examine the extent to which metal–metal bonding is optimized in the three isoelectronic compounds Nb_2Se, Ta_2Se, and Ta_2S, we have performed band structure calculations using the extended Hückel method (*29, 30*). Parameters for these calculations are given in Table V. The Densities of States (DOS) for all three materials are similar—the metal *d* bands are occupied with 4 electrons per metal center, as expected for group V elements with an average oxidation state of +1. None of the materials has a band gap and they are expected to be metallic, in accord with our expectations based on their structures (*31, 32*). We will dispense with an examination of the DOS curves and instead focus upon the crystal orbital overlap population (COOP) plots for each compound for levels in the *d* band region. In such plots the bonding (or antibonding) character of band orbitals is graphically displayed since a COOP curve is just a DOS curve in which the value of the DOS at each energy is weighted by the magnitude of the overlap population between a given pair of atoms in the structure. Thus, a COOP curve can be constructed for any pair of atoms in the structure. In Fig. 8, we have plotted averaged *M–M* COOP

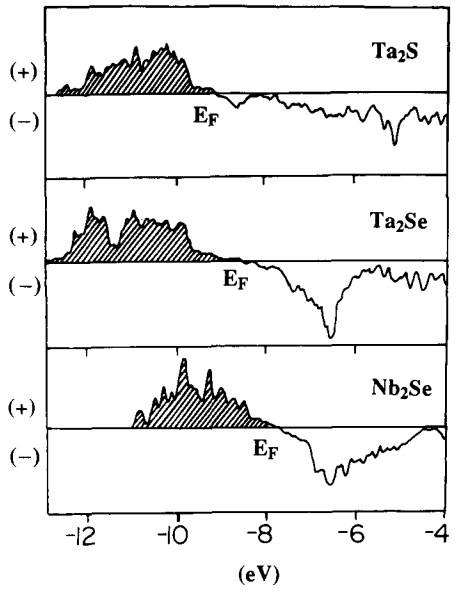

FIG. 8. Averaged crystal orbital overlap population (COOP) curves are plotted from top to bottom for Ta_2S, Ta_2Se, and Nb_2Se. Energy increases from left to right and the occupied levels for each system are shown shaded. Note the extent to which these compounds optimize *M–M* bonding.

curves in which the contribution by each symmetry unique bond enters with a weight proportional to the relative number of such bonds.

The notable general feature of these results is the closeness with which the Fermi level divides the bonding and antibonding crystal orbitals, i.e., all bonding levels are occupied and antibonding levels are vacant. This feature, when added to the results of calculations for numerous other metal-rich materials, suggests the strong constraint on structure that "COOP optimization" (i.e., optimization of metal–metal bonding) seems to provide (*4, 23, 33–42*). This has been particularly true for compounds with low-dimensional metal–metal bonded arrays. For a compound with more (or fewer) valence electrons that was otherwise chemically similar (say, "Zr_2S"), any of these structures would seem to be disfavored. Yao, Miller, and Franzen found essentially the same result for the Ta_2Se-like structure and have examined the issue of Nb vs Ta site preferences in the $(Ta,Nb)_4S_2$ layered compound as well (*32*).

As satisfying as this result seems, we see that Nature may find many structures that satisfy the "requirement" that such metal-rich compounds adopt structures which optimize the metal–metal bonding. All three materials are isoelectronic, all have different structures. While atomic size differences seem to be an important factor when comparing Ta_2S and Ta_2Se, the difference in the Nb_2Se and Ta_2Se structures is presently inexplicable. Computations demonstrating "how good the bonding is" can still be inadequate for predicting structure. These refractory materials have large cohesive energies and both the theoretical analysis and experimental facts indicate how small the "structure-determining" fraction of the cohesive energy may be.

These cautionary remarks are just as important when considering the issue of phase stability, where our ability to make confident predictions is practically nonexistent. We will find no convincing rationalization in the electronic structure for the low-temperature disproportionation of Ta_2S, as compared with the apparent low-temperature stability of Ta_2Se. We must conclude that even if the practically impossible goal of calculating low-temperature stabilities (enthalpies) for systems such as these were within reach, many interesting materials would still be missed!

Concluding Remarks

Dichalcogenides of tantalum are studied extensively for their layered structures and intercalation properties (*43 ,44*). The present study shows that in the Ta–S–Se and Ta–Nb–S systems new compounds exist with Ta_2Se-like layer structures that have robustly metallic regions separating the bcc van der Waals layers. Although Ta_2Se itself is a seemingly attractive material for intercalation, such chemistry will be hampered by the compound's air sensitivity. The materials $Ta_2S_{1-x}Se_x$ with higher sulfur content are less air-sensitive, while layered materials in the Ta–Nb–S system are indefinitely air-stable at room temperature, making these systems more attractive hosts. Work is underway in our laboratory to develop this chemistry.

We have also shown that nearly 80% of the selenium can be replaced with sulfur in high-temperature preparations while retaining the bcc based layered structure of Ta_2Se, whereas substitution of selenium into the $^1_\infty[Ta_5Ta]$ chain-based structures of Ta_2S and Ta_3S_2 is precluded due to size constraints. Previous work showed that vanadium can substitute for both peripheral antiprismatic site and central metal chain of the $^1_\infty[Ta_5Ta]$ skeleton of Ta_6S, and chromium prefers only the latter site—this was rationalized on the basis of radii effects and thermodynamic considerations (*7*). The present study rules out niobium substitution into ei-

ther of these sites; instead, the presence of niobium seems to favor the formation of Ta_2Se-like layer compounds.

Acknowledgments

We thank the donors of the Petroleum Research Fund, administered by the American Chemical Society, for their partial support of this research via Grant 20546-G3. We gratefully acknowledge the support of the National Science Foundation for its support through a Presidential Young Investigator Award (Grant DMR-8858151), and the Robert A. Welch Foundation for its support through Grant A-1132. We thank Dr. R. N. Guillemette in the Department of Geology at Texas A&M for providing his expertise in microprobe analysis, and Dr. Joe Reibenspies for assistance in the single crystal study. We extend thanks to H. F. Franzen and co-workers for providing a preprint detailing results of their investigations.

References

1. H. F. Franzen and J. G. Smeggil, *Acta Crystallogr. Sect. B* **B25,** 1736 (1969).
2. H. F. Franzen and J. G. Smeggil, *Acta Crystallogr. Sect. B* **B26,** 125 (1970).
3. B. Harbrecht, *J. Less-Common Met.* **138,** 225 (1988).
4. T. Hughbanks, *Prog. Solid State Chem.* **19,** 329 (1989).
5. H. Wada and M. Onoda, *Mater. Res. Bull.* **24,** 191 (1989).
6. S.-J. Kim, K. S. Nanjundaswamy, and T. Hughbanks, *Inorg. Chem.* **30,** 159 (1991).
7. B. Harbrecht and H. F. Franzen, *Z. Anorg. Allg. Chem.* **551,** 74 (1987).
8. B. Harbrecht and H. F. Franzen, *J. Less-Common Met.* **113,** 349 (1985).
9. B. Harbrecht, *J. Less-Common Met.* **124,** 125 (1986).
10. B. Harbrecht, *J. Less-Common Met.* **141,** 59 (1988).
11. M. E. Badding and F. J. DiSalvo, *Inorg. Chem.* **29,** 3952 (1990).
12. M. Potel, R. Chevrel, M. Sergent, J. C. Armici, M. Decroux, and O. Fischer, *Acta Crystallogr. Sect. B* **B36,** 1545 (1980).
13. M. Potel, R. Chevrel, and M. Sergent, *J. Solid State Chem.* **35,** 286 (1980).
14. B. Harbrecht, *Angew. Chem. Int. Ed. Engl.* **28,** 1660 (1989).
15. B. R. Conard, L. J. Norrby, and H. F. Franzen, *Acta Crystallogr. Sect. B* **B25,** 1729 (1969).
16. A. Nylund, *Acta Chem. Scand.* **20,** 2393 (1966).
17. X. Yao and H. F. Franzen, *J. Am. Chem. Soc.* **113,** 1426 (1991).
18. X. Yao and H. F. Franzen, *J. Solid State Chem.* **86,** 88 (1990).
19. G. M. Sheldrick, "SHELXTL-PLUS, an Integrated System for Solving, Refining, and Displaying Crystal Structures from Diffraction Data," Göttingen, Germany (1988).
20. J. A. Ibers and W. C. Hamilton, *in* "International Tables for X-ray Crystallography," Kynoch Press, Birmingham, England (1974).
21. N. Walker and D. Stuart, *Acta Crystallogr. Sect. A* **A39,** 158 (1983).
22. F. Gronvold, A. Kjekshus, and F. Raaum, *Acta Crystallogr.* **14,** 930 (1961).
23. A. Simon, *Angew. Chem. Int. Ed. Engl.* **20,** 1 (1981).
24. R. Berger, P. Phavanantha, and M. Mongkolsuk, *Acta Chem. Scand., Ser. A.* **34,** 77 (1980).
25. B. Harbrecht, S. R. Schmidt, and H. F. Franzen, *J. Solid State Chem.* **53,** 113 (1984).
26. H. F. Franzen, *Prog. Solid State Chem.* **12,** 1 (1978).
27. J. D. Corbett, *J. Solid State Chem.* **39,** 56 (1981).
28. R. D. Shannon, *Acta Crystallogr. Sect. A* **A32,** 751 (1976).
29. R. Hoffmann and W. N. Lipscomb, *J. Chem. Phys.* **37,** 2872 (1962).
30. R. Hoffmann, *J. Chem. Phys.* **39,** 1397 (1963).
31. T. Hughbanks, *in* "Inorganometallic Chemistry" (T. Fehlner, Ed.), Chapter 7, p 289.
32. X. Yao, G. J. Miller, and H. F. Franzen, submitted for publication.
33. T. Hughbanks and R. Hoffmann, *J. Am. Chem. Soc.* **105,** 1150 (1983).
34. T. Hughbanks and R. Hoffmann, *J. Am. Chem. Soc.* **105,** 3528 (1983).
35. J. K. Burdett and T. Hughbanks, *J. Am. Chem. Soc.* **106,** 3101 (1984).
36. T. Hughbanks and J. D. Corbett, *Inorg. Chem.* **28,** 631 (1989).
37. R. Chevrel, *in* "Crystal Chemistry and Properties of Materials with Quasi-One-Dimensional Structures" (J. Rouxel, Ed.), Reidel, New York (1986).
38. D. G. Adolphson and J. D. Corbett, *Inorg. Chem.* **15,** 1820 (1976).
39. C. C. Torardi and R. E. McCarley, *J. Am. Chem. Soc.* **101,** 1963 (1979).
40. C. C. Torardi and R. E. McCarley, *Inorg. Chem.* **24,** 476 (1985).
41. R. E. McCarley, *Polyhedron* **5,** 51 (1986).
42. A. Simon, *Angew. Chem. Int. Ed. Engl.* **27,** 160 (1988).
43. F. J. DiSalvo, G. W. Hull, L. H. Schwartz, J. M. Voorhoeve, and J. V. Waszczak, *J. Chem. Phys.* **59,** 1922 (1973).
44. M. S. Whittingham, *Prog. Solid State Chem.* **12,** 41 (1978).